AGU PUBLICATIONS

Geophysical Research Letters

RESEARCH LETTER

10.1002/2017GL073338

Key Points:
- We observe a 78 MPa stress drop for the 2016 M_w 5.2 Borrego Springs earthquake with a maximum slip of over 2.5 m
- The 97% of the >12,000 precisely located aftershocks occur more than 1 rupture length from the slip area and suggest a complete stress drop
- The seismic efficiency is estimated to be 15−26%

Supporting Information:
- Supporting Information S1

Correspondence to:
Z. E. Ross,
zross@gps.caltech.edu

Citation:
Ross, Z. E., H. Kanamori, and E. Hauksson (2017), Anomalously large complete stress drop during the 2016 M_w 5.2 Borrego Springs earthquake inferred by waveform modeling and near-source aftershock deficit, *Geophys. Res. Lett.*, *44*, 5994–6001, doi:10.1002/2017GL073338.

Received 4 MAR 2017
Accepted 5 MAY 2017
Accepted article online 8 MAY 2017
Published online 17 JUN 2017

Anomalously large complete stress drop during the 2016 M_w 5.2 Borrego Springs earthquake inferred by waveform modeling and near-source aftershock deficit

Z. E. Ross[1], H. Kanamori[1], and E. Hauksson[1]

[1]Seismological Laboratory, California Institute of Technology, Pasadena, California, USA

Abstract The 2016 M_w 5.2 Borrego Springs earthquake occurred in the trifurcation area of the San Jacinto Fault Zone and generated more than 23,000 aftershocks. We analyze source properties of this earthquake along with 12,487 precisely located aftershock hypocenters to obtain an unusually detailed view of the rupture process and energy budget for this moderate earthquake. Source time functions are obtained using an empirical Green's function approach and are inverted for a slip distribution on the fault plane. The rupture propagated unilaterally to the northwest over a distance of 1.8 km, resulting in clear directivity signals. Two asperities are identified and the maximum slip is 2.54 m, resulting in a static stress drop of 78.2 MPa. Over 97% of the aftershocks occur more than 1 rupture length from the slip area. We conclude that the Borrego Springs earthquake had a complete stress drop and estimate the seismic efficiency to be 15–26%.

1. Introduction

The San Jacinto Fault Zone (SJFZ) is a key structural element of the Southern California plate boundary area. It is a right-lateral strike-slip system that is diverse in seismicity rates [e.g., *Sanders and Kanamori*, 1984], geometric complexity [*Sharp*, 1967], and heat flow, [e.g., *Doser and Kanamori*, 1986] along strike. It also represents a significant contribution to the seismic hazard in Southern California, having produced 11 events with $M > 6$ in the past 120 years [*Kagan et al*., 2006]. In the central section of the SJFZ, the main Clark Fault splits into three subparallel faults, with the Buck Ridge to the northeast and the Coyote Creek Fault to the southwest (Figure 1). This region, which is often called the trifurcation area, is the most seismically active part of Southern California, having produced more than 10% of the earthquakes listed in the Southern California Seismic Network (SCSN) catalog since 2000 [*Southern California Earthquake Data Center* (*SCEDC*), 2013]. Most of these earthquakes have occurred inside a deep, seismogenic damage zone composed of interlaced faults and cracks [*Ross et al*., 2017]. These nearly orthogonal structures produce earthquakes with both strike-slip and normal faulting mechanisms [*Sharp*, 1975; *Mori*, 1993; *Kurzon et al*., 2014; *Ross et al*., 2017]. Adding to the complexity, the trifurcation area has also produced 10 main shock events with $M_w > 4$ since 2000, and 4 of these had $M_w > 5$ [*SCEDC*, 2013].

On 10 June 2016, the M_w 5.2 Borrego Springs earthquake occurred inside the trifurcation area on the Clark Fault (Figure 1) and produced more than 25,000 aftershocks in the following 2 weeks, with the magnitude of completeness estimated around −0.7 [*Ross et al*., 2017]. In this study, we determine the slip distribution, stress drop, and the energy budget of the Borrego Springs earthquake using high-quality recordings from more than 100 local stations. We combine the high-resolution aftershock hypocenters and the rupture process to get an unusually detailed look at the state of stress and seismic energy budget for a moderate-sized earthquake.

2. Data

We use seismic data recorded by the regional network (CI), plate boundary observatory (PB), ANZA network (AZ), a dense local PASSCAL deployment (YN) in and around the SJFZ [*Vernon and Ben-Zion*, 2010], and UCSB (SB) networks in Southern California for two events: the 2016 M_w 5.2 main shock (SCSN-ID:37374687; 10 June 2016 08:04:39) and a smaller M_L 3.37 event that occurred on 17 July 2014 (SCSN-ID:15527617; 17 July 2014 14:24:34). The preliminary data set contains 104 stations within 100 km of the main shock. For stations within 40 km of the hypocenter, accelerometer data were generally used, while for stations further out, broadband stations were used. The best estimate of the main shock hypocentral depth is 12.0 km. The main shock focal

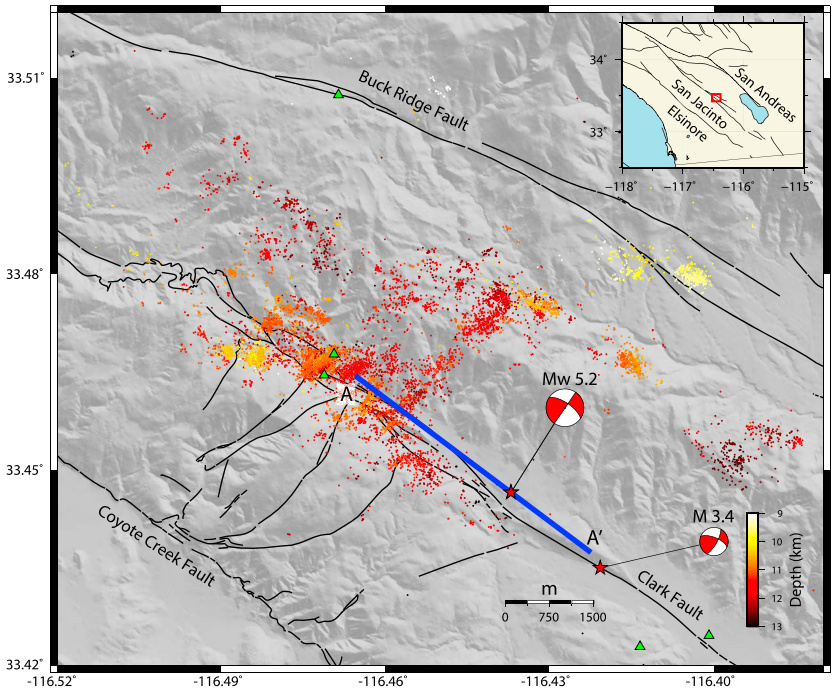

Figure 1. Map of the SJFZ trifurcation area and 12,487 events of the 2016 Borrego Springs sequence. Blue line indicates the fault plane used in Figure 3.

mechanism used in this study was determined by *Ross et al*. [2017], which has a strike of 304°, dip of 68°, and rake of 179°. The empirical Green's function (EGF) focal mechanism was determined using the method of *Yang et al*. [2012].

The seismicity data used in this study were produced and relocated by *Ross et al*. [2017] with a template matching approach [*Shelly et al*., 2016]. The catalog contains 25,392 events, of which 12,487 have the highest-quality locations and are the events used in this study (Figure 1). All phase picks were made by SCSN analysts [*SCEDC*, 2013].

3. Methods and Results

3.1. Determining the Slip Distribution

We solve for a slip distribution of the Borrego Springs main shock using a method that is conceptually similar to the method of *Mori and Hartzell* [1990]. First, a smaller nearby event with a similar focal mechanism is selected as an empirical Green's function (EGF) to deconvolve and thus remove the common propagation and site effects for a given station. *P* waves for both events were windowed starting 0.5 s before the pick and had a total window length of 2.5 s. The deconvolution was performed in the time domain using the procedure of *Kikuchi and Kanamori* [1982] and updated by *Ligorría and Ammon* [1999]. Each record was visually inspected to confirm that the deconvolution yielded a clear source time function (STF) with a relatively simple time history and verified that the forward prediction reliably could reproduce the observed seismogram. The deconvolution procedure included a smoothing operation that was equivalent to a 6 Hz low-pass filter, as significant noise appears above this frequency value at most stations (supporting information Figure S2). Applying this procedure to all records results in 43 STFs remaining from the initial set of 104 stations. The EGF and main shock hypocenters are separated by 2 km. We tested numerous other events as EGFs and found that event 15527617 yielded the cleanest STFs at the most stations.

The STFs for all stations are shown in Figure 2 sorted by azimuth. For azimuths near the strike of the fault in the northwest direction (~300°), the source duration is short (~0.5 s) and the STFs display a single main pulse. In the opposite direction, two main pulses are clearly visible, with a total source duration that is almost 1.5 s for some stations. For the range of azimuths in between these two orientations, the source duration is

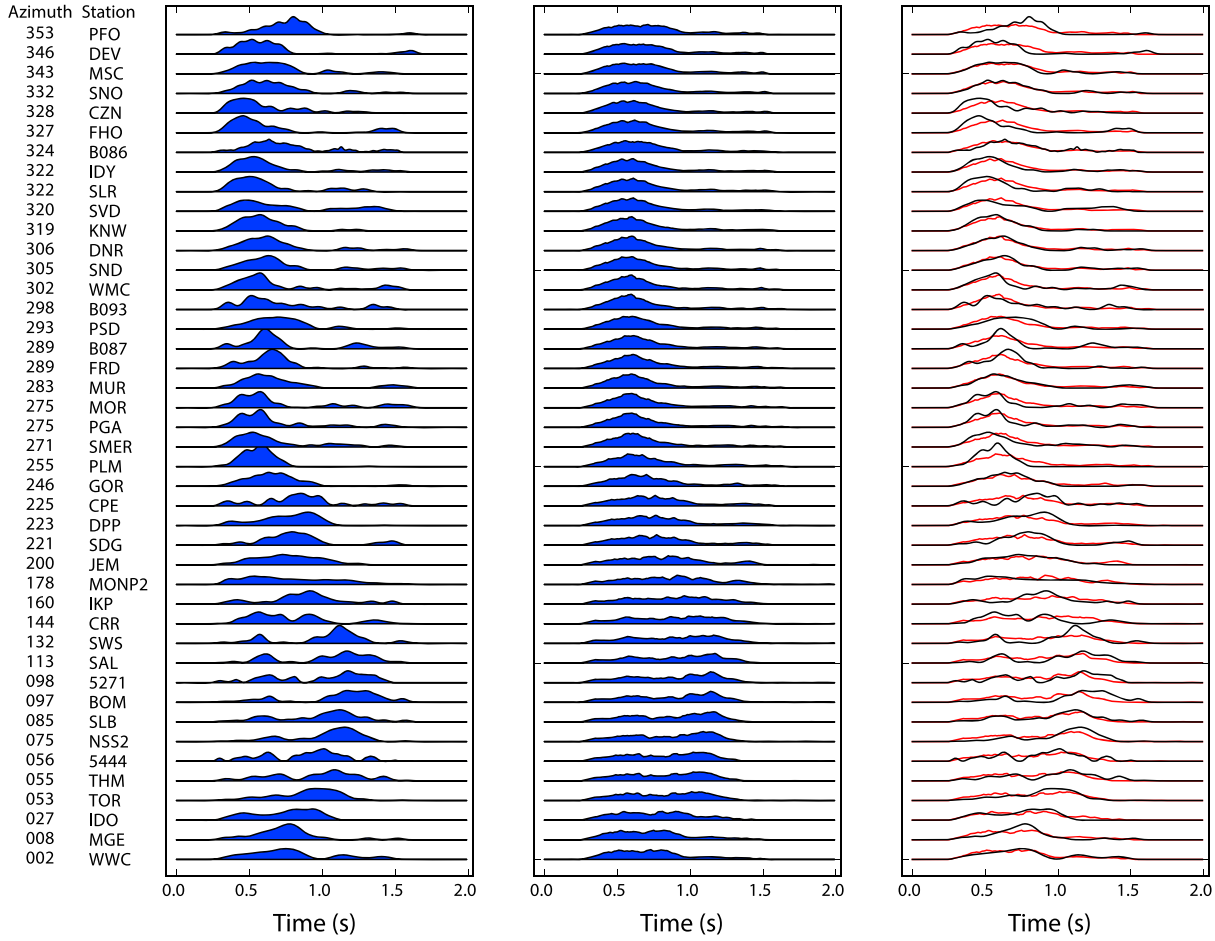

Figure 2. Source time functions at different stations. (left column) Observed source time functions and (middle column) the corresponding best fitting source time functions. (right column) Both the observed (black) and synthetic (red) source time functions together. Note the two distinct pulses over southeastern azimuths (55–132°) and single short pulse over northwestern azimuths (255–320°), characteristic of directivity effects.

approximately 0.8–0.9 s. These features are diagnostic of rupture directivity to the northwest along the Clark strand of the SJFZ. A clear directivity to the NW is also found using a spectral-based analysis of the type discussed by *Ross and Ben-Zion* [2016] (Figure S1).

We next invert the STFs for a slip distribution. First, a square grid with dimensions 3.6 km is created with grid spacing of 300 m, strike of 304°, and dip of 68°. The area underneath each STF is then normalized to have seismic moment equal to 7×10^{16} N m. We use the multiple time window linear inversion method to solve for the slip distribution [*Hartzell and Heaton*, 1983],

$$d = Gm, \tag{1}$$

where d is a vector containing the concatenated STFs from all stations, G is a matrix containing the triangles for each subfault and station, and m is a vector containing the concatenated slip values for each triangle at each subfault. A nonnegativity constraint was imposed in the inversion [*Lawson and Hanson*, 1995]. Five triangles are used for each cell with a half duration of 0.05 s, and the triangles are made to overlap by the same amount. We used a constant rupture velocity of 2.4 km/s (0.7 v_s) for the inversion and calculated the relative delay times between each source node and a given station using a 1-D layered model for Southern California [*Hadley and Kanamori*, 1977]. Other rupture velocities were tested in the range 0.6–0.9 v_s, and the details are discussed in the subsequent section. Figure 2b shows the best fitting STFs, while Figure 2c shows the best fitting STFs in red against the data STFs in black. The slip model fits the data well and captures the two main slip patches and northwest rupture directivity as seen from the STFs alone.

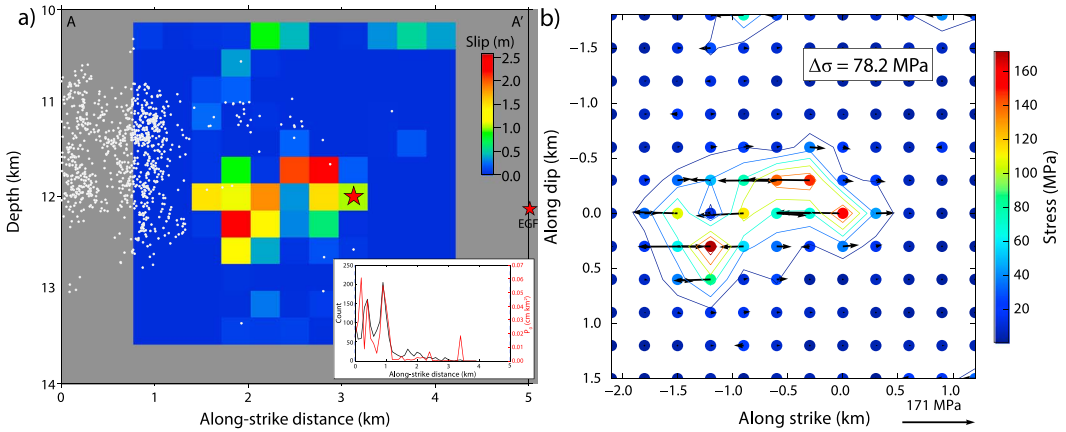

Figure 3. (a) Slip distribution of Borrego Springs main shock projected onto fault plane A–A′. Aftershock hypocenters within 500 m of the fault plane are indicated by white circles. Main shock hypocenter is indicated by the red star. The rupture propagated unilaterally to the northwest. The maximum slip is determined to be 2.54 m. Two asperities are visible, which can also be identified in the STFs directly for southeastern azimuths. Inset contains the number of aftershocks and seismic potency within 500 m of the fault plane in 100 m bins. (b) The stress drop is determined to be 78.2 MPa averaged over the rupture area using the method of *Noda et al.* [2013].

Figure 3a contains the slip distribution projected onto the vertical plane, without any smoothing included. After the rupture initiates, it propagates unilaterally to the northwest. The total rupture length is approximately 1.8 km, and the width of the rupture at its widest point is 1.2 km. The maximum slip over the rupture area is 2.54 m. The slip distribution consists of two asperities: a smaller one at the site of the hypocenter and a slightly larger one to the northwest, which contains the maximum slip.

We tested the different parameters extensively to assess the overall robustness of the solution. The triangle duration was varied over the range 0.025–0.05 s, and there was generally no change to the slip distribution, with the two asperities both remaining in the same place and having similar slip values. We also varied the grid size from 100 to 400 m and observed that the model was generally unstable when the grid spacing was 200 m or less, scattering slip across the fault plane. The low-pass filter was varied over the 2–10 Hz range, and it was found to not affect the source duration. The number of triangles used in the inversion does not change the slip distribution, and the parameter that has the most influence on the slip distribution is the rupture velocity. We cannot discern any significant difference in waveform fit when using rupture velocities from 0.6 to 0.9 v_s, which leads to stress drop values in the range 49.4–85.0 MPa. For rupture velocities 0.7 v_s and larger, two asperities are present in the slip models. In all cases, the stress drop is unusually high and the northwest rupture directivity is present. Therefore, while the rupture velocity itself is poorly constrained, the most important features of the inversion are still present regardless of the final value used.

3.2. Analysis of the Aftershock Spatial Distribution

The Borrego Springs earthquake produced more than 1500 aftershocks ($-0.2 < M < 3.75$) within 2 weeks that were detected by the SCSN from routine network processing. Five of the eight aftershocks with $M > 3$ had normal faulting mechanisms, while the main shock itself had a right-lateral strike-slip mechanism. Many of the aftershocks occurred on a northeast trending structure located to the northwest of the main shock hypocenter (Figure 1), which became active for the first time since at least 1981 [*Hauksson et al.*, 2012]. Using a template matching approach, *Ross et al.* [2017] identified more than 23,000 additional aftershocks during this same period; however, less than 1% of all events occurred within 2 km of the main shock hypocenter (Figure 1).

Aftershocks within 500 m of the fault plane are shown as white dots in Figure 3a, while the along-strike seismic potency is plotted in the figure inset. Here the scaling relation of *Ross et al.* [2016] was used to convert the local magnitudes into seismic potency. Only 4 out of 12,487 aftershocks occurred inside the rupture area, which is estimated from the grid elements with at least 0.5 m of slip. The aftershock distribution brackets the northwestern edge of the rupture area to within a few hundred meters. These events were determined to have relative location errors less than 162 m at the 95% confidence level.

3.3. Stress Drop and Energy Budget

We use the slip model directly to determine the static stress drop:

$$\Delta\sigma_E = \frac{\int_\Sigma \Delta\sigma \Delta u \, ds}{\int_\Sigma \Delta u \, ds}, \tag{2}$$

which is a weighted average of the (local) stress drop, $\Delta\sigma$, with the weights given by the slip, Δu [*Noda et al.*, 2013]. The stress is computed using whole space dislocations at each point of the grid (Figure 3b). The estimate of $\Delta\sigma_E$ is 78.2 MPa, which is about 2 orders of magnitude higher than what is typically observed for crustal earthquakes but similar to the value observed for the 2008 M_w 5.4 Chino Hills earthquake in Southern California [*Shao et al.*, 2012]. Rupture velocities in the range 0.6–0.9 v_s produce stress drop values in the range 49.4–85.0 MPa.

The STFs provide an opportunity to estimate the seismic energy released during the earthquake as well. Following *Vassiliou and Kanamori* [1982], we calculate the seismic energy, E_R, by directly integrating the STFs:

$$E_R = KM_0^2 I, \tag{3a}$$

$$K = \left[\left(1/15\pi p\alpha^5\right) + \left(1/10\pi p\beta^5\right)\right], \tag{3b}$$

$$I = 2\int_0^\infty \left|\dot{S}(f)\right|^2 df. \tag{3c}$$

where $\dot{S}(f)$ denotes the Fourier transform of the source time function, $\dot{s}(t)$, normalized to unit area, at a given station. The values used for α, β, and ρ were 5.8 km/s, 3.4 km/s, and 2700 kg/m^3, respectively. The integral in equation (3c) was calculated up to a value of 6 Hz separately for each station, based on the low-pass filter used during the deconvolution. The median seismic energy is therefore 1.25×10^{13} J. Assuming ω^{-2} scaling, 25% of the energy would be missing for a corner frequency of 1.2 Hz and cutoff frequency of 6 Hz, which raises this value to 1.67×10^{13} J. Using this value, the moment-scaled energy, $\varepsilon = E_R/M_0 = 2.4 \times 10^{-4}$. As shown in Figure S2, high-frequency noise affects the estimates of seismic energy. Similar computations with 2 Hz and 8 Hz low-pass filters for the deconvolution lead to values of 1.35×10^{13} J and 2.6×10^{13} J, respectively. The 8 Hz value appears to be is strongly affected by high-frequency noise, while the 2 Hz cutoff frequency may be too close to the corner frequency. Therefore, the 6 Hz low-pass filter seems to be a reasonable compromise.

The source dimension of this earthquake is constrained well from the combination of the aftershock and slip distribution. This allows us to estimate the stress drop within a factor of about 2. The availability of high-quality close-in stations enables us to estimate the radiated energy accurately within the available frequency bandwidth. Then the radiation efficiency,

$$\eta_R = \frac{E_R}{\Delta W_0} = \frac{2\mu}{\Delta\sigma_E}\left(\frac{E_R}{M_0}\right), \tag{4}$$

can be estimated as 0.15–0.26 corresponding to the range of $\Delta\sigma_E$ from 49 to 85 MPa. In the above equation, $\Delta W_0 = \frac{\Delta\sigma_E}{2\mu} M_0$ is the available strain energy. We note that the radiation efficiency, η_R, is not the same as the real seismic efficiency given by $\eta = E_R/\Delta W$, where ΔW is the total strain energy release given by $\Delta W = (\sigma_0 + \sigma_1) M_0/2\mu$. Here σ_0 and σ_1 are the initial and final (residual) stresses. Given the difficulty of determining the absolute stress with commonly available seismological methods, ΔW_0 is often used as the strain energy available for rupture propagation that is equal to the sum of E_R and the fracture energy E_G. Therefore, η_R is the ratio of the radiated energy to the sum of E_R and E_G. More details on this and some caveats are given in *Kanamori and Rivera* [2006]. For the 2016 Borrego Springs earthquake, the near absence of even small aftershocks in the rupture zone suggests a small residual stress σ_1. If this is the case, $\Delta\sigma = \sigma_0 - \sigma_1 \approx \sigma_0$, $\Delta W_0 \approx \Delta W$, and $\eta_R \approx \eta$. Then the relatively small η_R estimated for the 2016 Borrego Springs earthquake indicates that 74–85% of the strain energy was dissipated in mechanical and thermal processes fracturing the material near the slip patch, and only 15–26% of the released strain energy was radiated as seismic waves.

4. Discussion

The stress drop of the Borrego Springs earthquake is considerably larger than for most earthquakes. *Kanamori et al.* [1993] and *Hauksson et al.* [2008] determined shear wave pulse widths for earthquakes in the Los Angeles (LA) basin, which are summarized in Figure 4. We measured the shear wave pulse width of the Borrego Springs earthquake using four stations within 20° of the fault normal to minimize directivity

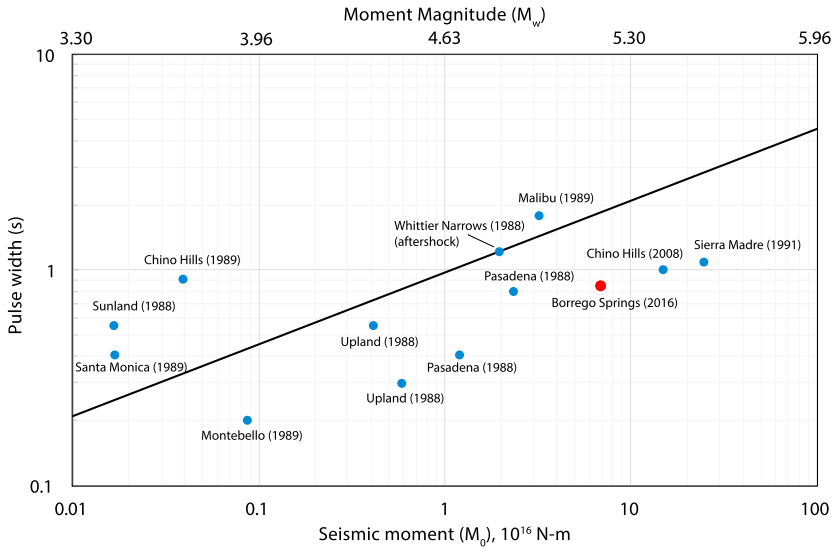

Figure 4. Shear wave pulse width measurements for Los Angeles basin earthquakes from *Kanamori et al.* [1993] and *Hauksson et al.* [2008]. The black line is a global trend from *Kanamori and Brodsky* [2004]. The pulse width for the 2016 Borrego Springs earthquake is denoted by the red circle and is about a factor of 2 shorter than for the average event with M_w 5.2. Many of the Los Angeles basin earthquakes have a similarly short pulse width, which may form their own group.

effects, with the average value shown as a red dot. We only selected stations within 30 km distance so that the effect of attenuation is negligible. The average pulse width for this event is about half of the average value for M_w 5.2 events and is near the lower bound of the trend shown in Figure 10 of *Kanamori and Brodsky* [2004]. The data set used by *Kanamori and Brodsky* [2004] includes events with M_w 2.0–8.2 from Japan (events with $M_w \leq 6$; M. Kikuchi, written communication, 2001) and some global events ($M_w > 6$). The pulse width of the Borrego Springs earthquake is, however, in line with a number of events with similar size, which occurred in the LA basin. *Hauksson et al.* [2008] suggested that these short pulse width events may form their own high stress drop group.

The Borrego Springs main shock shows strong unilateral directivity to the northwest along the Clark Fault strand of the SJFZ. *Ross and Ben-Zion* [2016] showed that the 11 March 2013 M_w 4.7 Borrego Springs earthquake also had strong directivity to the northwest. *Kurzon et al.* [2014] analyzed 800 small earthquakes in the trifurcation area using peak ground acceleration measurements and found that many showed evidence for northwest rupture propagation. These observations may be a manifestation of the bimaterial rupture hypothesis [*Weertman*, 1980; *Andrews and Ben-Zion*, 1997; *Ampuero and Ben-Zion*, 2008; *Brietzke and Ben-Zion*, 2006], which predicts that for a fault with a velocity contrast, the direction of slip in the more compliant medium is a preferred propagation direction. In the SJFZ trifurcation area, the northeast side of the Clark Fault is nominally faster [*Allam et al.*, 2014], resulting in a preferred rupture direction to the northwest, and this is consistent with all of these observations.

The relationship between the spatial distribution of aftershocks and the slip distribution has been discussed in numerous works [e.g., *Beroza and Spudich*, 1988; *Mendoza and Hartzell*, 1988; *Beroza*, 1991; *Hsu et al.*, 2006; *Sladen et al.*, 2010; *Wei et al.*, 2011]. In many past large earthquakes, the distribution of aftershocks shows anticorrelation with the slip distribution, such that the largest asperities typically have the lowest density of aftershocks. For the Borrego Springs earthquake, this is also observed (Figure 3 inset), with nearly all aftershocks occurring outside of the rupture area. In fact, 97% of all events are more than a full rupture length away from the northwestern edge of the rupture area. The lack of aftershocks within the rupture area most likely reflects a state of low residual stress.

Our analysis of the Borrego Springs earthquake indicates significant energy dissipation during faulting. This is in contrast with the situation for other faults such as the Punchbowl Fault, where very little energy is dissipated and slip occurs in an extremely narrow zone [*Chester et al.*, 2005]. The large energy dissipation for the 2016 event occurred over a small area, about 1.5 km in dimension, in the complex trifurcation area,

and the low efficiency may not be a general characteristic of larger earthquakes that occur on relatively simple fault segments. However, as the SJFZ is younger and more geometrically complex than the San Andreas Fault, with broad damage zones in the upper 5 km [*Allam et al*., 2014], it is also possible that there are systematic differences in the rupture process between these two fault systems.

The rupture process of the 2016 Borrego Springs earthquake exhibited a variety of interesting features for being only moderate in size. Some of these features—such as unilateral rupture directivity—are often viewed as primarily an issue for large earthquakes; the extent to which smaller events exhibit complex source effects is still not well understood [e.g., *Boatwright*, 2007; *Kane et al*., 2013]. With the amount of high-quality data recorded around the world increasing by the year, seismologists will be able to study the source properties of these smaller events in greater detail. Given their more frequent occurrence, moderate earthquakes have the potential to provide uniquely valuable insight into the source process.

5. Conclusions

We analyze the rupture process and energy budget of the 2016 M_w 5.2 Borrego Springs earthquake. An empirical Green's function approach was used to derive a slip distribution and estimate the seismic energy, stress drop, and radiation efficiency. The calculated stress drop of ~80 MPa is unusually large for a crustal earthquake, while the radiation efficiency is found to be relatively low. These quantities are well constrained by a prominent near-source aftershock deficit, which further allows us to estimate the seismic efficiency at 15–26%. Together, these observations suggest that most of the available strain energy went into fracturing and thermal processes, rather than seismic radiation.

Acknowledgments
We thank Zhongwen Zhan, Yehuda Ben-Zion, Marine Denolle, and an anonymous reviewer for their constructive comments. This research was supported by USGS/NEHRP grant G16AP00147; NSF award EAR-1550704; and by the Southern California Earthquake Center, which is funded by NSF Cooperative Agreement EAR-1033462 and USGS Cooperative Agreement G12AC20038. We used GMT from *Wessel et al*., [2013] to make the figures. We have used waveforms and parametric data from the Caltech/USGS Southern California Seismic Network (SCSN); doi:10.7914/SN/CI; stored at the Southern California Earthquake Center. doi:10.7909/C3WD3xH1. There are no real or perceived financial conflicts of interests for any author.

References

Allam, A. A., Y. Ben-Zion, I. Kurzon, and F. L. Vernon (2014), Seismic velocity structure in the Hot Springs and Trifurcation Areas of the San Jacinto Fault Zone, California, from double-difference tomography, *Geophys. J. Int.*, *198*, 978–999, doi:10.1093/gji/ggu176.

Ampuero, J.-P., and Y. Ben-Zion (2008), Cracks, pulses and macroscopic asymmetry of dynamic rupture on a bimaterial interface with velocity-weakening friction, *Geophys. J. Int.*, *173*, 674–692, doi:10.1111/j.1365-246X.2008.03736.x.

Andrews, D. J., and Y. Ben-Zion (1997), Wrinkle-like slip pulse on a fault between different materials, *J. Geophys. Res.*, *102*, 553–571, doi:10.1029/96JB02856.

Beroza, G. C. (1991), Near-source modeling of the Loma Prieta earthquake: Evidence for heterogeneous slip and implications for earthquake hazard, *Bull. Seismol. Soc. Am.*, *81*(5), 1603–1621.

Beroza, G. C., and P. Spudich (1988), Linearized inversion for fault rupture behavior: Application to the 1984 Morgan Hill, California, earthquake, *J. Geophys. Res.*, *93*, 6275–6296, doi:10.1029/JB093iB06p06275.

Boatwright, J. (2007), The persistence of directivity in small earthquakes, *Bull. Seismol. Soc. Am.*, *97*(6), 1850–1861.

Brietzke, G. B., and Y. Ben-Zion (2006), Examining tendencies of in-plane rupture to migrate to material interfaces, *Geophys. J. Int.*, *167*, 807–819, doi:10.1111/j.1365-246X.2006.03137.x.

Chester, J. S., F. M. Chester, and A. K. Kronenberg (2005), Fracture surface energy of the Punchbowl Fault, San Andreas system, *Nature*, *437*, 133–136, doi:10.1038/nature03942.

Doser, D. I., and H. Kanamori (1986), Depth of seismicity in the Imperial Valley Region (1977–1983) and its relationship to heat flow, crustal structure and the October 15, 1979, earthquake, *J. Geophys. Res.*, *91*(B1), 675–688, doi:10.1029/JB091iB01p00675.

Hadley, D. H., and H. Kanamori (1977), Seismic structure of the Transverse Ranges, California, *Geol. Soc. Am. Bull.*, *88*(10), 1469–1478.

Hartzell, S. H., and T. H. Heaton (1983), Inversion of strong ground motion and teleseismic waveform data for the fault rupture history of the 1979 Imperial Valley, California, earthquake, *Bull. Seismol. Soc. Am.*, *73*(6A), 1553–1583.

Hauksson, E. H., K. Felzer, D. Given, M. Giveon, S. Hough, H. Kanamori, V. Sevilgen, S. Wei, and A. Yong (2008), Preliminary report on the 29 July 2008 M_w 5.4 Chino Hills, eastern Los Angeles Basin, California, earthquake sequence, *Seismol. Res. Lett.*, *79*(6), doi:10.1785/gssrl.79.6.855.

Hauksson, E. H., W. Yang, and P. M. Shearer (2012), Waveform relocated earthquake catalog for Southern California (1981 to June 2011), *Bull. Seismol. Soc. Am.*, *102*(5), 2239–2244, doi:10.1785/0120120010.

Hsu, Y.-J., M. Simons, J.-P. Avouac, J. Galetzka, K. Sieh, M. Chlieh, D. Natawidjaja, L. Prawirodirdjo, and Y. Bock (2006), Frictional afterslip following the 2005 Nias-Simeulue Earthquake, Sumatra, *Science*, *312*, 1921–1926, doi:10.1126/science.1126960.

Kagan, Y. Y., D. D. Jackson, and Y. Rong (2006), A new catalog of Southern California earthquakes, 1800–2005, *Seismol. Res. Lett.*, *77*, 30–38.

Kanamori, H. and Rivera, L. (2006), Energy partitioning during an earthquake, in *Earthquakes: Radiated Energy and the Physics of Faulting*, edited by R. Abercrombie et al., pp. 3–13, AGU, Washington, D. C., doi:10.1029/170GM03.

Kanamori, H., and E. Brodsky (2004), The physics of earthquakes, *Rep. Prog. Phys.*, *67*(8), 1429–1496.

Kanamori, H., J. Mori, E. Hauksson, T. H. Heaton, L. K. Hutton, and L. M. Jones (1993), Determination of earthquake energy release and M_L using TERRAscope, *Bull. Seismol. Soc. Am.*, *83*(2), 330–346.

Kane, D. L., P. M. Shearer, B. P. Goertz-Allmann, and F. L. Vernon (2013), Rupture directivity of small earthquakes at Parkfield, *J. Geophys. Res. Solid Earth*, *118*, 212–221, doi:10.1029/2012JB009675.

Kikuchi, M., and H. Kanamori (1982), Inversion of complex body waves, *Bull. Seismol. Soc. Am.*, *72*(2), 491–506.

Kurzon, I., F. L. Vernon, Y. Ben-Zion, and G. Atkinson (2014), Ground motion prediction equations in the San Jacinto Fault Zone: Significant effects of rupture directivity and fault zone amplification, *Pure and Applied Geophysics*, *171*(11), 3045–3081, doi:10.1007/s00024-014-0855-2.

Lawson, C. L., and R. J. Hanson (1995) *Solving Least Squares Problems*, pp. 1–337, Society for Industrial and Applied Mathematics, Philadelphia, Pa.
Ligorría, J. P., and C. J. Ammon (1999), Iterative deconvolution and receiver-function estimation, *Bull. Seismol. Soc. Am.*, *89*(5), 1395–1400.
Mendoza, C., and S. H. Hartzell (1988), Aftershock patterns and main shock faulting, *Bull. Seismol. Soc. Am.*, *78*(4), 1438–1449.
Mori, J. (1993), Fault plane determinations for three small earthquakes along the San Jacinto Fault, California: Search for cross faults, *J. Geophs. Res.*, *98*(B10), 17,711–17,722, doi:10.1029/93JB01229.
Mori, J., and S. Hartzell (1990), Source inversion of the 1988 Upland, California, earthquake: Determination of a fault plane for a small event, *Bull. Seismol. Soc. Am.*, *80*(3), 507–518.
Noda, H., N. Lapusta, and H. Kanamori (2013), Comparison of average stress drop measures for ruptures with heterogeneous stress change and implications for earthquake physics, *Geophys. J. Int.*, *193*(3), 1691–1712, doi:10.1093/gji/ggt074.
Ross, Z. E., and Y. Ben-Zion (2016), Towards reliable automated estimates of earthquake source properties from body wave spectra, *J. Geophys. Res. Solid Earth*, *121*, 4390–4407, doi:10.1002/2016JB013003.
Ross, Z. E., Y. Ben-Zion, M. C. White, and F. L. Vernon (2016), Analysis of earthquake body wave spectra for potency and magnitude values: Implications for magnitude scaling relations, *Geophys. J. Int.*, *207*, 1158–1164, doi:10.1093/gji/ggw327.
Ross, Z. E., E. Hauksson, and Y. Ben-Zion (2017), Abundant off-fault seismicity and orthogonal structures in the San Jacinto Fault Zone, *Sci. Adv.*, *3*(3), e1601946), doi:10.1126/sciadv.1601946.
Sanders, C. O., and H. Kanamori (1984), A seismotectonic analysis of the Anza Seismic Gap, San Jacinto Fault Zone, Southern California, *J. Geophys. Res.*, *89*(B7), 5873–5890, doi:10.1029/JB089iB07p05873.
Southern California Earthquake Data Center (SCEDC) (2013), Southern California Earthquake Data Center, California Institute of Technology, doi:10.7909/C3WD3xH1.
Shao, G., C. Ji, and E. Hauksson (2012), Rupture process and energy budget of the 29 July 2008 M_w 5.4 Chino Hills, California, earthquake, *J. Geophys. Res.*, *117*, B07307, doi:10.1029/2011JB008856.
Sharp, R. V. (1967), San Jacinto Fault Zone in the Peninsular Ranges of Southern California, *Geol. Soc. Am. Bull.*, *78*(6), 705–730.
Sharp, R. V. (1975), En echelon fault patterns of the San Jacinto Fault Zone, in San Andreas Fault in Southern California (ed. J. C. Cromwell), *Spec. Rep. Calif. Div. Mines Geol.*, *118*, 147–154.
Shelly, D. R., W. L. Ellsworth, and D. P. Hill (2016), Fluid-faulting evolution in high definition: Connecting fault structure and frequency-magnitude variations during the 2014 Long Valley Caldera, California, earthquake swarm, *J. Geophys. Res. Solid Earth*, *121*, 1776–1795, doi:10.1002/2015JB012719.
Sladen, A., H. Tavera, M. Simons, J. P. Avouac, A. O. Konca, H. Perfettini, L. Audin, E. J. Fielding, F. Ortega, and R. Cavagnoud (2010), Source model of the 2007 M_w 8.0 Pisco, Peru earthquake: Implications for seismogenic behavior of subduction megathrusts, *J. Geophys. Res.*, *115*, B02405, doi:10.1029/2009JB006429.
Vassiliou, M. S., and H. Kanamori (1982), The energy release in earthquakes, *Bull. Seismol. Soc. Am.*, *72*(2), 371–387.
Vernon, F. L., and Y. Ben-Zion (2010), San Jacinto Fault Zone Experiment. International Federation of Digital Seismograph Networks. Other/Seismic Network, doi:10.7914/SN/YN_2010.
Weertman, J. (1980), Unstable slippage across a fault that separates elastic media of different elastic constants, *J. Geophys. Res.*, *85*(B3), 1455–1461, doi:10.1029/JB085iB03p01455.
Wei, S., et al. (2011), Superficial simplicity of the 2010 El Mayor-Cucapah earthquake of Baja California in Mexico, *Nat. Geosci.*, *4*, 615–618, doi:10.1038/ngeo1213.
Wessel, P., W. H. F. Smith, R. Scharroo, J. F. Luis, and F. Wobbe (2013), Generic Mapping Tools: Improved version released, *Eos Trans. AGU*, *94*, 409–410.
Yang, W., E. Hauksson, and P. M. Shearer (2012), Computing a large refined catalog of focal mechanisms for Southern California (1981–2010): Temporal stability of the style of faulting, *Bull. Seismol. Soc. Am.*, *102*(3), 1179–1194, doi:10.1785/0120110311.